Pairing properties in relativistic mean field models obtained from effective field theory

M. Del Estal, M. Centelles, X. Viñas, and S. K. Patra
Departament d'Estructura i Constituents de la Matèria, Facultat de Física, Universitat de Barcelona, Diagonal 647, E-08028 Barcelona, Spain
(Received 22 November 2000; published 22 March 2001)

We apply recently developed effective field theory nuclear models in mean field approximation (parameter sets G1 and G2) to describe ground-state properties of nuclei from the valley of β stability up to the drip lines. For faster calculations of open-shell nuclei we employ a modified BCS approach which takes into account quasibound levels owing to their centrifugal barrier, with a constant pairing strength. We test this simple prescription by comparing with available Hartree-plus-Bogoliubov results. Using the new effective parameter sets we then compute separation energies, density distributions, and spin-orbit potentials in isotopic (isotonic) chains of nuclei with magic neutron (proton) numbers. The new forces describe the experimental systematics similarly to conventional nonlinear $\sigma-\omega$ relativistic force parameters like NL3.

DOI: 10.1103/PhysRevC.63.044321 PACS number(s): 21.60.−n, 21.10.Dr, 21.30.Fe

I. INTRODUCTION

The relativistic field theory of hadrons known as quantum hadrodynamics (QHD) has become a very useful tool for describing bulk and single-particle properties of nuclear matter and finite nuclei in the mean field approximation [1–4]. Compared with the nonrelativistic approach to the nuclear many-body problem, the relativistic model explicitly includes the mesonic degrees of freedom and treats the nucleons as Dirac particles. At the mean field (Hartree) level, nucleons interact in a relativistic covariant way by exchanging virtual mesons: an isoscalar-vector ω meson, an isoscalar-scalar σ meson, and an isovector-vector ρ meson. With these ingredients the mean field treatment of QHD automatically takes into account the spin-orbit force, the finite range, and the density dependence of the nuclear force. Adjusting some coupling constants and meson masses from the properties of a small number of finite nuclei, the relativistic mean field (RMF) model produces excellent results for binding energies, root-mean-square radii, quadrupole and hexadecapole deformations, and other properties of spherical and deformed nuclei [5,6].

The original linear $\sigma-\omega$ model of Walecka [7] was complemented with cubic and quartic nonlinearities of the σ meson [8] (nonlinear $\sigma-\omega$ model) to improve the results for the incompressibility and for finite nuclei. Since these models were proposed to be renormalizable, the scalar self-interactions were limited to a quartic polynomial and scalar-vector or vector-vector interactions were not allowed. Recently, and inspired by effective field theory (EFT), Furnstahl, Serot, and Tang [9,10] abandoned the idea of renormalizability and extended the RMF theory by including other nonlinear scalar-vector and vector-vector self-interactions as well as tensor couplings [4,9–13].

The EFT Lagrangian has an infinite number of terms since it contains all the nonrenormalizable couplings consistent with the underlying QCD symmetries. Therefore it is mandatory to develop a suitable scheme of expansion and truncation. At normal nuclear densities the scalar (Φ) and vector (W) meson fields are small compared with the nucleon mass (M), and they vary slowly with position in finite nuclei. This indicates that the ratios Φ/M, W/M, $|\boldsymbol{\nabla}\Phi|/M^2$, and $|\boldsymbol{\nabla}W|/M^2$ can be used as the expansion parameters. With the help of the concept of naturalness, it is then possible to compute the contributions of the different terms in the expansion and to truncate the effective Lagrangian at a given level of accuracy [4,10,12,13]. None of the couplings should be arbitrarily dropped out to the given order without a symmetry argument.

References [10,12,13] have shown that it suffices to go to fourth order in the expansion. At this level one recovers the standard nonlinear $\sigma-\omega$ model plus a few additional couplings, with 13 free parameters in all. These parameters have been fitted (parameter sets G1 and G2) to reproduce some observables of magic nuclei [10]. The fits display naturalness (i.e., all coupling constants are of the order of unity when written in appropriate dimensionless form), and the results are not dominated by the last terms retained. This evidence confirms the utility of the EFT concepts and justifies the truncation of the effective Lagrangian at the first lower orders.

Recent applications of the models based on EFT include studies of pion-nucleus scattering [14] and of the nuclear spin-orbit force [15], as well as calculations of asymmetric nuclear matter at finite temperature with the G1 and G2 sets [16]. In a previous work [17] we have analyzed the impact of each one of the new couplings introduced in the EFT models on the nuclear matter saturation properties and on the nuclear surface properties. In Ref. [18] we have looked for constraints on the new parameters by demanding consistency with Dirac-Brueckner-Hartree-Fock (DBHF) calculations and the properties of finite nuclei. In recent years a large amount of work has been devoted to measuring masses of nuclei far from stability [19]. This body of experimental data has been used as a benchmark to test the predictions of the currently existent (relativistic and nonrelativistic) nuclear effective forces [20]. This fact motivates us to investigate in the present work the behavior of the parameter sets G1 and

G2 derived from EFT in regions far from the stability line.

To study ground-state properties of spherical open-shell nuclei one has to take into account the pairing correlations. Relativistic mean field calculations near the β-stability line have usually included pairing in a constant gap BCS approximation [5,21,22], with the gaps fitted to empirical odd-even mass differences. This approach works properly when the main effect of the pairing correlations is a smearing of the Fermi surface. Since the BCS pairing energy diverges for large momenta, a cutoff has to be introduced in the pairing channel to simulate phenomenologically the finite range of the particle-particle force. The limitations of this simple BCS method appear when one deals with nuclei far from the β-stability line. Close to the drip lines the Fermi level falls near the particle continuum and it is known that the BCS model does not provide a correct description of the coupling between bound and continuum states [23,24]. In the nonrelativistic framework this difficulty was overcome by the unified description of the mean field and the pairing correlations provided by the Hartree-Fock-Bogoliubov (HFB) theory [25,26], with Skyrme [23,24] or Gogny forces [27].

The same unified treatment was developed by Kucharek and Ring [28] in the relativistic framework. However, a quantitative description of the pairing correlations in nuclei cannot be achieved with relativistic mean field parametrizations because the meson exchange forces are not properly adapted to large momentum transfer [28,29]. Later, Ring and co-workers [29–32] have used the RMF interaction for the particle-hole channel plus the pairing part of the Gogny force [27] (with the D1S parameters [33]) for the particle-particle channel, in relativistic Hartree-plus-Bogoliubov (RHB) calculations. Other authors have employed a density-dependent zero-range pairing force [34] instead of the Gogny pairing force [35,36].

Recent calculations with nonrelativistic Skyrme forces and a zero-range force in the particle-particle channel have shown that a BCS approach is able to provide a good qualitative estimate of the drip lines if some quasibound states due to their centrifugal barrier (plus the Coulomb barrier for protons) are included in the calculation [37–39]. In this work we will use a similar BCS approach with quasibound states to approximately take into account the effects of the continuum contributions near the drip lines. We will employ a constant pairing strength which can be considered as a simplification of the zero-range pairing force and which gives similar results to those obtained with a delta force for spherical nuclei [40].

The paper is organized as follows. We summarize the mean field approximation to the EFT nuclear model in the second section. In the third section we describe our modified BCS approach with quasibound states, and perform some calculations to test its possibilities and limitations by comparing with Bogoliubov results available from the literature. The fourth section is devoted to the detailed study with the EFT parametrizations G1 and G2 of properties such as separation energies, particle densities, and spin-orbit potentials of nuclei belonging to chains of isotopes (isotones) with magic proton (neutron) number. Our conclusions are laid out in the last section.

II. RELATIVISTIC MEAN FIELD APPROACH FROM EFFECTIVE FIELD THEORY

The effective field theory approach to QHD has been developed in the recent years. The theory and the equations for nuclear matter and finite nuclei can be found in the literature [4,9,10] and here we shall only outline the formalism. We start from Ref. [9] where the field equations were derived from an energy density functional containing Dirac baryons and classical scalar and vector mesons. This functional can be obtained from the effective Lagrangian in the Hartree approximation, but it can also be considered as an expansion in terms of the ratios of the meson fields and their gradients to the nucleon mass of a general energy density functional that contains the contributions of correlations within the spirit of density functional theory [4,10].

According to Refs. [4,10] the energy density for finite nuclei can be written as

$$
\begin{aligned}
\mathcal{E}(\mathbf{r}) = \sum_{\alpha}\ \varphi_{\alpha}^{\dagger}\Bigg\{ & -i\boldsymbol{\alpha}\cdot\boldsymbol{\nabla} + \beta(M-\Phi) + W + \frac{1}{2}\tau_3 R + \frac{1+\tau_3}{2}A \\
& - \frac{i}{2M}\beta\boldsymbol{\alpha}\cdot\left(f_v\boldsymbol{\nabla}W + \frac{1}{2}f_\rho\tau_3\boldsymbol{\nabla}R + \lambda\boldsymbol{\nabla}A\right) \\
& + \frac{1}{2M^2}(\beta_s+\beta_v\tau_3)\Delta A\Bigg\}\varphi_\alpha + \left(\frac{1}{2} + \frac{\kappa_3}{3!}\frac{\Phi}{M} + \frac{\kappa_4}{4!}\frac{\Phi^2}{M^2}\right) \\
& \times \frac{m_s^2}{g_s^2}\Phi^2 - \frac{\zeta_0}{4!}\frac{1}{g_v^2}W^4 + \frac{1}{2g_s^2}\left(1+\alpha_1\frac{\Phi}{M}\right)(\boldsymbol{\nabla}\Phi)^2 \\
& - \frac{1}{2g_v^2}\left(1+\alpha_2\frac{\Phi}{M}\right)(\boldsymbol{\nabla}W)^2 - \frac{1}{2}\left(1+\eta_1\frac{\Phi}{M}+\frac{\eta_2}{2}\frac{\Phi^2}{M^2}\right) \\
& \times \frac{m_v^2}{g_v^2}W^2 - \frac{1}{2g_\rho^2}(\boldsymbol{\nabla}R)^2 - \frac{1}{2}\left(1+\eta_\rho\frac{\Phi}{M}\right)\frac{m_\rho^2}{g_\rho^2}R^2 \\
& - \frac{1}{2e^2}(\boldsymbol{\nabla}A)^2 + \frac{1}{3g_\gamma g_v}A\Delta W + \frac{1}{g_\gamma g_\rho}A\Delta R, \qquad (1)
\end{aligned}
$$

where the index α runs over all occupied states $\varphi_\alpha(\mathbf{r})$ of the positive energy spectrum, $\Phi \equiv g_s\phi_0(\mathbf{r})$, $W \equiv g_v V_0(\mathbf{r})$, $R \equiv g_\rho b_0(\mathbf{r})$, and $A \equiv eA_0(\mathbf{r})$. Variation of the energy density (1) with respect to $\varphi_\alpha^\dagger$ and the meson fields gives the Dirac equation fulfilled by the nucleons and the meson field equations, which are solved self-consistently by numerical iteration. We refer the reader to Ref. [10] for the expressions of the variational equations.

The terms with g_γ, λ, β_s, and β_v take care of effects related with the electromagnetic structure of the pion and the nucleon (see Ref. [10]). Specifically, the constant g_γ concerns the coupling of the photon to the pions and the nucleons through the exchange of neutral vector mesons. The experimental value is $g_\gamma^2/4\pi = 2.0$. The constant λ is needed to reproduce the magnetic moments of the nucleons. It is defined by

TABLE I. Dimensionless parameters and saturation properties of the sets G1 and G2 based on EFT and of the RMF set NL3.

	G1	G2	NL3
m_s/M	0.540	0.554	0.541
$g_s/4\pi$	0.785	0.835	0.813
$g_v/4\pi$	0.965	1.016	1.024
$g_\rho/4\pi$	0.698	0.755	0.712
κ_3	2.207	3.247	1.465
κ_4	−10.090	0.632	−5.668
ζ_0	3.525	2.642	0.0
η_1	0.071	0.650	0.0
η_2	−0.962	0.110	0.0
η_ρ	−0.272	0.390	0.0
α_1	1.855	1.723	0.0
α_2	1.788	−1.580	0.0
$f_v/4$	0.108	0.173	0.0
$f_\rho/4$	1.039	0.962	0.0
β_s	0.028	−0.093	0.0
β_v	−0.250	−0.460	0.0
a_v (MeV)	−16.14	−16.07	−16.24
ρ_∞ (fm^{-3})	0.153	0.153	0.148
K (MeV)	215.0	215.0	271.5
M^*_∞/M	0.634	0.664	0.595
J (MeV)	38.5	36.4	37.40

$$\lambda = \frac{1}{2}\lambda_p(1+\tau_3) + \frac{1}{2}\lambda_n(1-\tau_3), \tag{2}$$

with $\lambda_p = 1.793$ and $\lambda_n = -1.913$ the anomalous magnetic moments of the proton and the neutron, respectively. The terms with β_s and β_v contribute to the charge radii of the nucleon [10].

In this work we will employ the EFT parameter sets G1 and G2 of Refs. [4,10]. The masses of the nucleon and the ω and ρ mesons take their experimental values: $M = 939$ MeV, $m_v = 782$ MeV, and $m_\rho = 770$ MeV. The 13 parameters m_s, g_s, g_v, g_ρ, η_1, η_2, η_ρ, κ_3, κ_4, ζ_0, f_v, α_1, and α_2 were fitted by a least-squares optimization procedure to 29 observables (binding energies, charge form factors, and spin-orbit splittings near the Fermi surface) of the nuclei ^{16}O, ^{40}Ca, ^{48}Ca, ^{88}Sr, and ^{208}Pb, as described in Ref. [10]. The constants β_s, β_v, and f_ρ were then chosen to reproduce the experimental charge radii of the nucleon. The fits yielded two best, distinct parameter sets (G1 and G2) with essentially the same χ^2 value [10].

We report in Table I the values of the parameters and the saturation properties of G1 and G2. One observes that the fitted parameters differ significantly between both interactions. For example, G2 presents a positive value of κ_4, as opposed to G1 and to many of the most successful RMF parametrizations, such as the NL3 parameter set [41]. Formally a negative value of κ_4 is not acceptable because the energy spectrum then has no lower bound [42]. Furthermore, the wrong sign in the Φ^4 coupling constant may cause troubles in obtaining stable solutions in light nuclei like ^{12}C. We note that the value of the effective mass at saturation M^*_∞/M in the EFT sets (~ 0.65) is somewhat larger than the usual value in the RMF parameter sets (~ 0.60). This fact is related with the presence of the tensor coupling f_v of the ω meson to the nucleon, which has an important bearing on the spin-orbit force [10,15,17].

One should mention that the EFT perspective also has been helpful to elucidate the empirical success of the usual nonlinear $\sigma-\omega$ models that incorporate less couplings (just up to cubic and quartic self-interactions of the scalar field): the EFT approach accounts for the success of these RMF models and provides an expansion scheme at the mean field level and for going beyond it [4,10,12]. In practice it has been seen that the mean field phenomenology of bulk and single-particle nuclear observables does not constrain all of the new parameters of the EFT model unambiguously. That is, the constants of the EFT model are underdetermined by the observables currently included in the fits and different parameter sets with low χ^2 (comparable to G1 and G2) can be found [10,12–14]. However, the extra couplings could prove to be very useful for the description of further observables. Indeed, for densities above the normal saturation density, and owing to the additional nonlinear couplings, the EFT models are able [18] to give an equation of state and nuclear matter scalar and vector self-energies in much better agreement with the microscopic Dirac-Brueckner-Hartree-Fock (DBHF) predictions than the standard nonlinear $\sigma-\omega$ parametrizations (the latter completely fail in following the DBHF trends as the nuclear density grows [18,22]).

The sets G1 and G2 were fitted including center-of-mass corrections in both the binding energy and the charge radius. Therefore we will utilize the same prescription of Ref. [10] in our calculations with G1 and G2, namely, a correction

$$E_{\text{c.m.}} = \frac{17.2}{A^{1/5}}\,\text{MeV} \tag{3}$$

to the binding energy and a correction

$$-\frac{3}{4}\frac{1}{(2MAE_{\text{c.m.}})}\,\text{fm}^2 \tag{4}$$

to the mean-square charge radius.

III. PAIRING CALCULATION

It is well known that pairing correlations have to be included in any realistic calculation of medium and heavy nuclei. In principle the microscopic HFB theory should be used for this purpose. However, for pairing calculations of a broad range of nuclei not too far from the β-stability line, a simpler procedure is usually considered in which a seniority potential acts between time-reversed orbitals. In this section we want to discuss and test a straightforward improvement of this simple approximation to be able to describe in addition nuclei near the drip lines, at least on a qualitative level. Without the complications intrinsic to a full Bogoliubov calculation, our faster approximation will allow us later on to perform

extensive calculations of chains of isotopes and isotones with the relativistic parameter sets.

The pairing correlation will be considered in the BCS approach [25,26]. One assumes that the pairing interaction $v_{\rm pair}$ has nonzero matrix elements only between pairs of nucleons invariant under time reversal:

$$\langle \alpha_2 \tilde{\alpha}_2 | v_{\rm pair} | \alpha_1 \tilde{\alpha}_1 \rangle = -G, \tag{5}$$

where $|\alpha\rangle = |nljm\rangle$ and $|\tilde{\alpha}\rangle = |nlj-m\rangle$ (with $G>0$ and $m>0$). Most often the BCS calculations in the RMF model have been performed using a constant gap approach [5,21,22]. Instead, here we choose a seniority-type interaction with a constant value of G for pairs belonging to the active pairing shells.

The contribution of the pairing interaction to the total energy, for each kind of nucleon (neutrons or protons), is

$$E_{\rm pair} = -G\left\{ \sum_{\alpha>0} [n_\alpha(1-n_\alpha)]^{1/2} \right\}^2 - G\sum_{\alpha>0} n_\alpha^2, \tag{6}$$

where n_α is the occupation probability of a state with quantum numbers $\alpha \equiv \{nljm\}$ and the sum is restricted to positive values of m. One has

$$n_\alpha = \frac{1}{2}\left[1 - \frac{\varepsilon_\alpha - \mu}{\sqrt{(\varepsilon_\alpha - \mu)^2 + \Delta^2}} \right]. \tag{7}$$

The Lagrange multiplier μ is called the chemical potential and the gap Δ is defined by

$$\Delta = G\sum_{\alpha} [n_\alpha(1-n_\alpha)]^{1/2}. \tag{8}$$

As usual the last term in Eq. (6) will be neglected. It is not a very important contribution and its only effect is a renormalization of the pairing energies [25,26].

Assuming constant pairing matrix elements (5) in the vicinity of the Fermi level one gets [25,26]

$$\frac{G}{2}\sum_{\alpha>0} \frac{1}{\sqrt{(\varepsilon_\alpha - \mu)^2 + \Delta^2}} = 1, \tag{9}$$

$$\frac{1}{2}\left[1 - \frac{\varepsilon_\alpha - \mu}{\sqrt{(\varepsilon_\alpha - \mu)^2 + \Delta^2}} \right] = A, \tag{10}$$

where A is the number of neutrons or protons involved in the pairing correlation. The solution of these two coupled equations allows one to find μ and Δ. Using Eqs. (7) and (8) the pairing energy for each kind of nucleon can be written as

$$E_{\rm pair} = -\frac{\Delta^2}{G}. \tag{11}$$

This simple approach breaks down for nuclei far from the stability line. The reason is that in this case the number of neutrons (for isotopes) or protons (for isotones) increases, the corresponding Fermi level approaches zero and the number of available levels above it is clearly reduced. Moreover, in this situation the particle-hole and pair excitations reach the continuum. Reference [23] showed that if one performs a BCS calculation using the same quasiparticle states as in a HFB calculation, then the BCS binding energies are close to the HFB ones but the rms radii (i.e., the single-particle wave functions) dramatically depend on the size of the box where the calculation is performed. This is due to the fact that there are neutrons (protons) that occupy continuum states for which the wave functions are not localized in a region, thus giving rise to an unphysical neutron (proton) gas surrounding the nucleus.

Recent nonrelativistic calculations near the drip lines with Skyrme forces [38,39] have shown that the above problem of the BCS approach can be corrected, in an approximate manner, by taking into account continuum effects by means of the so-called quasibound states, namely, states bound because of their own centrifugal barrier (centrifugal-plus-Coulomb barrier for protons). When the quasibound states are included in the BCS calculation (from now on a qb-BCS calculation), it is necessary to prevent the unrealistic pairing of highly excited states and to confine the region of influence of the pairing potential to the vicinity of the Fermi level. Instead of using a cutoff factor as in Ref. [38], in our calculations we will restrict the available space to one harmonic oscillator shell above and below the Fermi level.

In order to check this approach we have performed with the G1 parameter set ($G_n = 21/A$ MeV, see next section) calculations of the binding energy and rms radius of the ^{120}Sn and ^{160}Sn nuclei in boxes of sizes between 15 and 25 fm (as in the nonrelativistic calculations of Ref. [23]). The results taking into account the quasibound levels $1h_{9/2}$, $2f_{5/2}$, and $1i_{13/2}$ for ^{120}Sn, and $1i_{11/2}$ and $1j_{13/2}$ for ^{160}Sn, are compared in Fig. 1 with the output of a standard BCS calculation with only bound levels. It turns out that in the qb-BCS case the results are essentially independent of the size of the box where the calculations are carried out. When the quasibound levels are included the binding energies are larger than when only the bound levels are taken into account, due to the damping of the pairing correlation caused by disregarding the continuum states in the standard BCS calculation [23]. We also show in Fig. 1 the results of a BCS calculation using all bound and unbound levels (i.e., without restricting ourselves to quasibound levels) in the considered range. It is obvious that in this case the results are box dependent, as the binding energy and neutron rms radius of ^{160}Sn evidence.

Another test of the qb-BCS approach concerns the asymptotic behavior of the particle densities [24]. In Fig. 2 we display the radial dependence of the neutron density of ^{150}Sn (as in Ref. [24]) calculated with the G1 parameter set in boxes of radii between 15 and 25 fm. For large enough distances the density decreases smoothly when the size of the box increases (except very near of the edge, where the density suddenly drops to zero because of the $\varphi_\alpha = 0$ boundary condition). This means that no neutron gas surrounding the nucleus has appeared. In a Bogoliubov calculation the asymptotic behavior of the particle density is governed by the square of the lower component of the single-quasiparticle wave function corresponding to the lowest quasiparticle en-

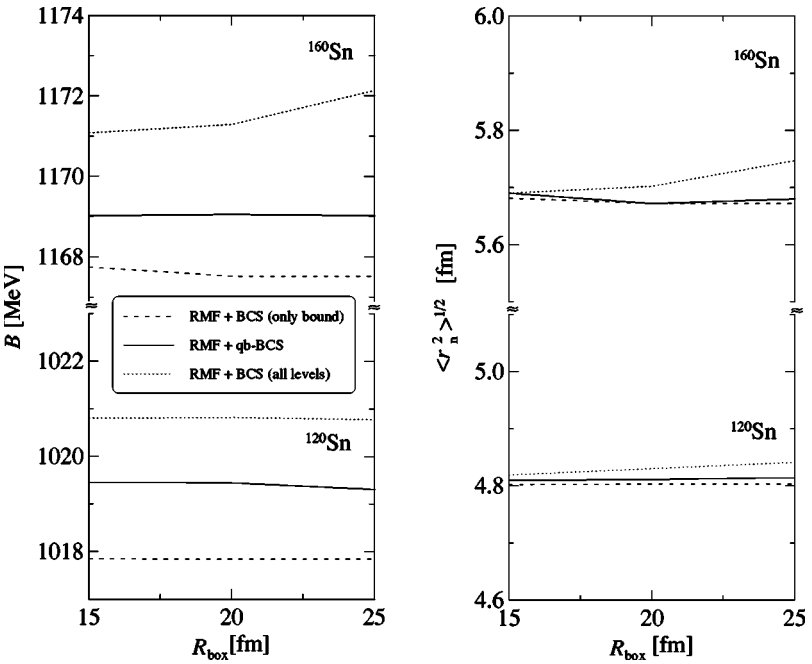

FIG. 1. Dependence of the binding energy (left) and neutron rms radius (right) of the nuclei ^{120}Sn and ^{160}Sn on the size of the box used in the calculations. Solid, dashed, and dotted lines correspond to a BCS approach including quasibound levels, only bound levels, and all available levels, respectively. The results are for the G1 parameter set.

ergy [24]. This asymptotic behavior is displayed by the (almost straight) dotted line in Fig. 2. It can be seen that the density obtained with our approach decreases more slowly than the RHB density, i.e., asymptotically the qb-BCS density is not able to follow the RHB behavior. This coincides with the conclusion of Ref. [24] (see Fig. 19 of that work) where nonrelativistic HFB densities are compared for large distances with the densities obtained in the qb-BCS approach with a state-dependent pairing [37].

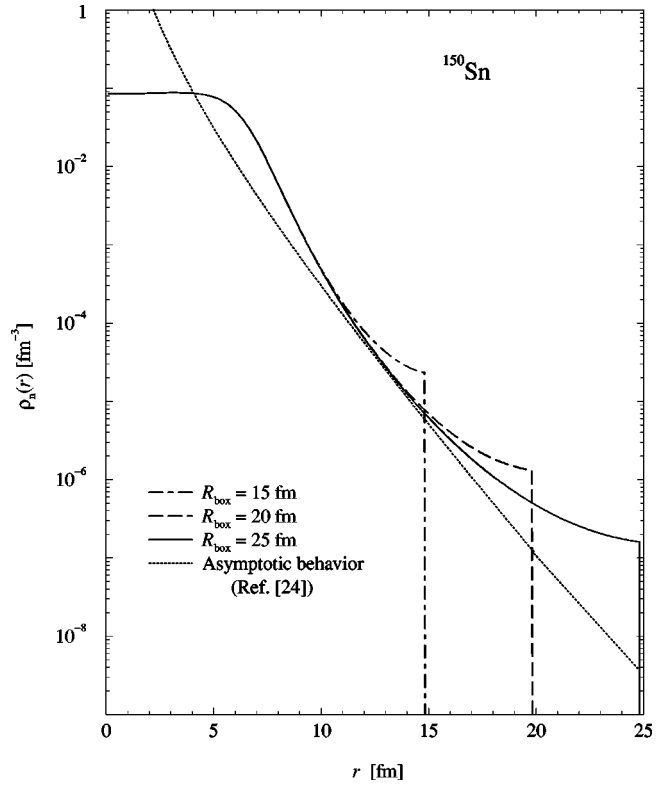

FIG. 2. Neutron density of ^{150}Sn for different sizes of the box used in the qb-BCS calculations (for the set G1). The dotted line denotes the asymptotic behavior expected from a Bogoliubov calculation [24].

Although the qb-BCS densities do not display the right asymptotic behavior, it was conjectured in Ref. [24] that such an approach could allow one to compute properties of nuclei much closer to the drip lines than in a standard BCS calculation. Very recently, RHB calculations up to the drip lines of the two-neutron separation energy S_{2n} for nickel isotopes [35] and of the charge and neutron rms radii for tin isotopes [36] have been carried out using the NL-SH parameter set [43] plus a density-dependent zero-range pairing force. We have repeated these calculations with our qb-BCS method for both isotopic chains (with a pairing interaction strength $G_n = 22.5/A$ in the case of NL-SH).

We display the values of the S_{2n} separation energies for the Ni chain in Fig. 3(a). The RHB calculation predicts the drip line at the isotope ^{100}Ni and shows shell effects at $N = 28$ and 50 (and to a minor extent at $N = 70$). These features are well predicted by our simpler qb-BCS calculation. The differences between these qb-BCS and RHB results also come in part from the different pairing forces used in the calculations. To investigate this point we show in Fig. 3(b) the neutron pairing energy obtained in our approach [Eq. (11)] for the isotopes of the Ni chain. It vanishes at $N = 28$, 50, and 70, in agreement with the shell structure shown in Fig. 3(a) by the S_{2n} separation energies. The largest pairing energies are found in the middle of two closed shells and they are enhanced by increasing N. Figure 3(b) can be compared with the RHB values displayed in Fig. 2 of Ref. [35]. The tendencies are the same, though the qb-BCS pairing energies are slightly larger than in the RHB calculation. In Fig. 4 we draw our results for the radii of the Sn isotopes, and compare them with the RHB values. In the case of the charge radii the agreement is excellent. The neutron radii obtained

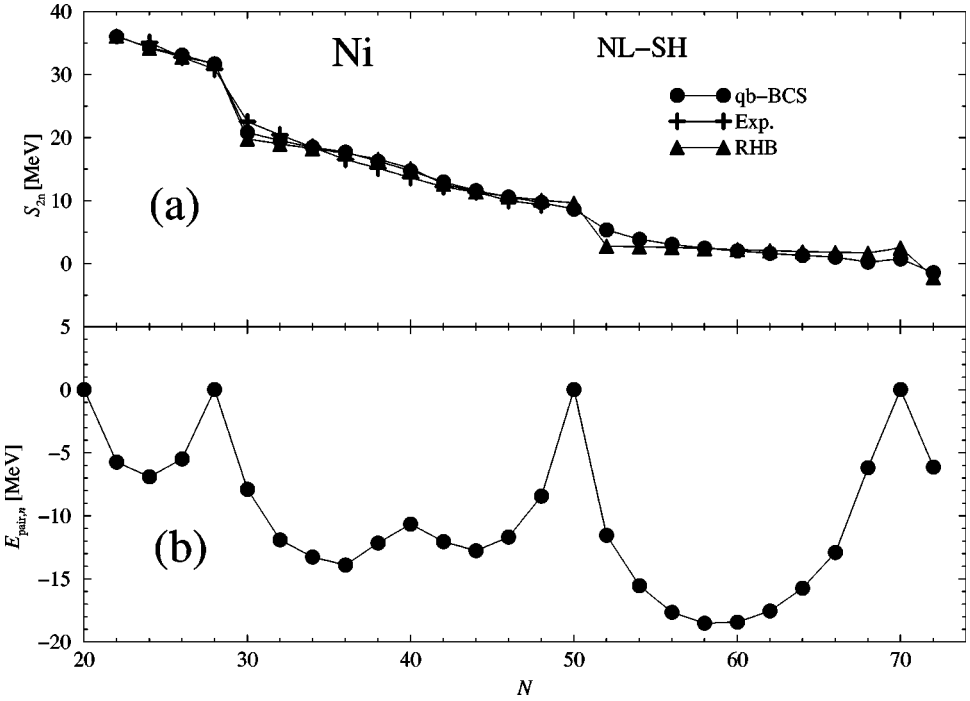

FIG. 3. (a) The two-neutron separation energies for Ni isotopes calculated in the qb-BCS approach are compared with the RHB results of Ref. [35] and with experiment. (b) The neutron pairing energy obtained in the qb-BCS approach. The results are for the set NL-SH.

in our method closely follow the behavior of the RHB neutron radii and the kink at $N=132$ is qualitatively reproduced.

We have furthermore computed the binding energies of nuclei of the $N=20$ isotonic chain for which RHB results exist with the NL3 parameter set [31]. We present the extracted two-proton separation energies S_{2p} in Table II. The agreement between the qb-BCS and RHB approaches again is very good. In both models the last stable nucleus is ^{46}Fe, as in experiment. Notice that in the present case the first levels with positive energy correspond to those of the pf shell. Due to the Coulomb barrier all these levels become quasibound in our approach, and it is expected that they will lie close to the canonical levels. This explains the goodness of the qb-BCS energies for this isotonic chain.

From the previous comparisons we see that the simple qb-BCS calculation is able to reasonably follow the main trends of the more fundamental RHB pairing calculation. One can also conclude that the consideration of quasibound states in the BCS approach is, actually, a key ingredient to eliminate the spurious nucleon gas arising near the drip lines.

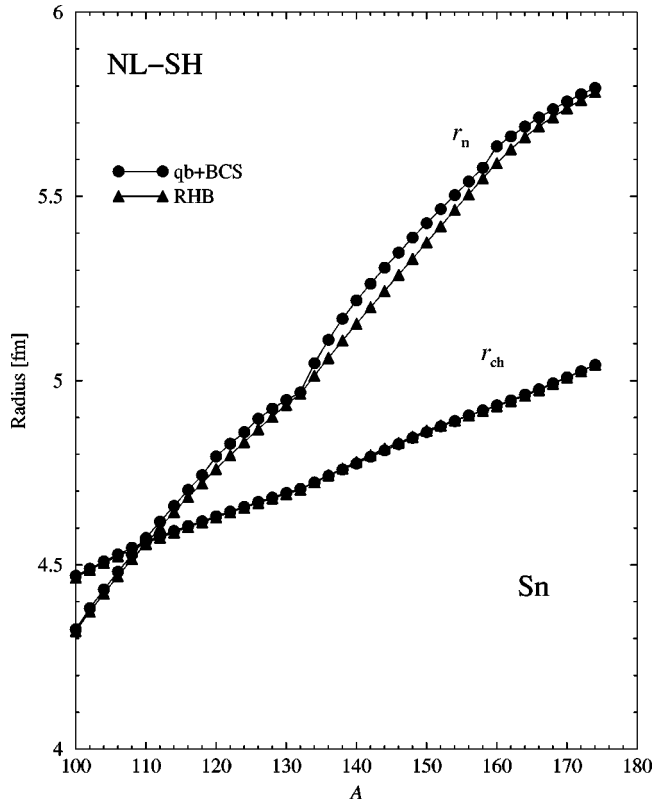

FIG. 4. Charge and neutron rms radii of Sn isotopes in qb-BCS and RHB [36] calculations performed with the NL-SH set.

IV. RESULTS FOR EFT PARAMETER SETS

We want to analyze the ability of the G1 and G2 parameter sets based on effective field theory [4,10] to describe

TABLE II. RHB and qb-BCS two-proton separation energies (in MeV) of some $N=20$ isotones calculated with the NL3 parameter set.

S_{2p}	RHB	qb-BCS	exp
^{36}S	23.56	23.05	25.28
^{38}Ar	19.36	18.97	18.35
^{40}Ca	14.65	15.46	14.99
^{42}Ti	6.36	6.70	4.86
^{44}Cr	3.30	3.31	3.08
^{46}Cr	0.60	0.54	0.21
^{48}Ni	−2.33	−2.21	

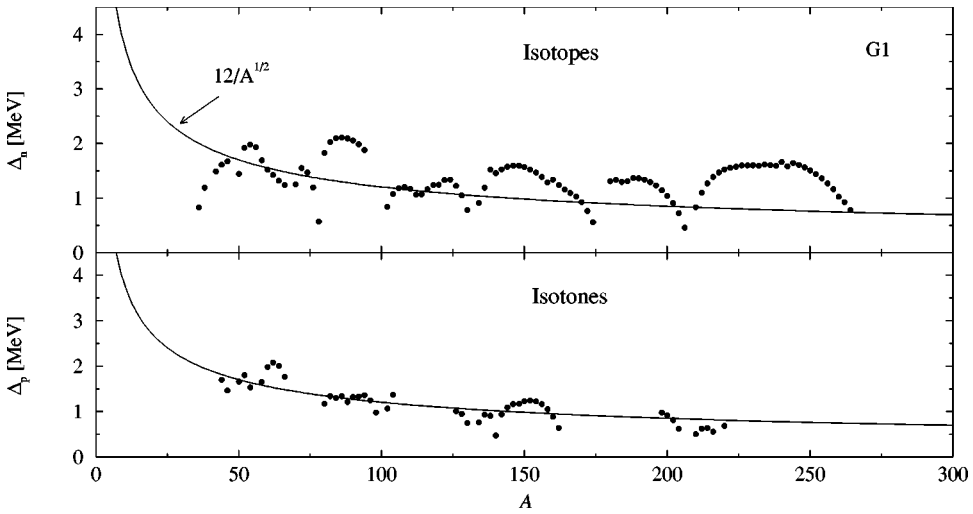

FIG. 5. The state-independent pairing gaps predicted by our qb-BCS approach for Ni, Sn, and Pb isotopes (top) and for $N=28$, 50, 82, and 126 isotones (bottom). The G1 set has been used. The empirical average curve $12/\sqrt{A}$ [44] is depicted by a solid line.

nuclear properties far from the stability line, i.e., far from the region where the parameters were fitted. To our knowledge such calculations have not been explored so far. We will contrast the results with experiment and with those predicted by the NL3 set, that we take as one of the best representatives of the usual RMF model with only scalar self-interactions.

As indicated, we shall use a schematic pairing with a state-independent matrix element $G_\tau = C_\tau/A$, where C_τ is a constant and $\tau = n,p$ for neutrons or protons, respectively. We fix the constant C_n for neutrons by looking for the best agreement of our calculation with the known experimental binding energies of Ni and Sn isotopes. Similarly, we determine C_p for protons from the experimental binding energies of the isotones of $N=28$ and $N=82$. The values obtained from this fit are $C_n=21$ MeV and $C_p=22.5$ MeV for the G1 set, $C_n=19$ MeV and $C_p=25$ MeV for G2, and finally $C_n=20.5$ MeV and $C_p=23$ MeV for NL3. Figure 5 shows that the neutron and proton state-independent gaps (Δ_n and Δ_p) predicted by our calculation with G1 are scattered around the empirical average curve $12/\sqrt{A}$ [44]. A similar picture is found with the parameter sets G2 and NL3.

A. Two-particle separation energies

In Fig. 6(a) we present the two-neutron separation energies S_{2n} for the chain of Ni isotopes. Clear shell effects arise at $N=28$ and 50. The three relativistic interactions (G1, G2, and NL3) slightly overestimate the shell effect at $N=28$ as compared with the experimental value, which also happens in more sophisticated RHB calculations with NL3 [30,32]. In our qb-BCS approach some disagreement with experiment is found for the $N=38$ and $N=40$ isotopes. Again, this also occurs in the RHB calculations of Refs. [30,32] with NL3. However, if we compare Fig. 6(a) with the results that we have shown in Fig. 3(a) for the NL-SH parameter set, we see that NL-SH achieves a better agreement with experiment for these $N=38$ and $N=40$ isotopes.

We stop our calculation towards the neutron drip line when the two-neutron separation energy vanishes or when the neutron chemical potential becomes positive. The fact that S_{2n} is not always zero at the drip line is connected with the quenching of the shell structure with N, which is a force-dependent property [24]. This effect is illustrated in Fig. 25 of Ref. [24] for HFB calculations with different nonrelativistic forces. We find similar situations with the considered relativistic sets in our qb-BCS calculations of separation en-

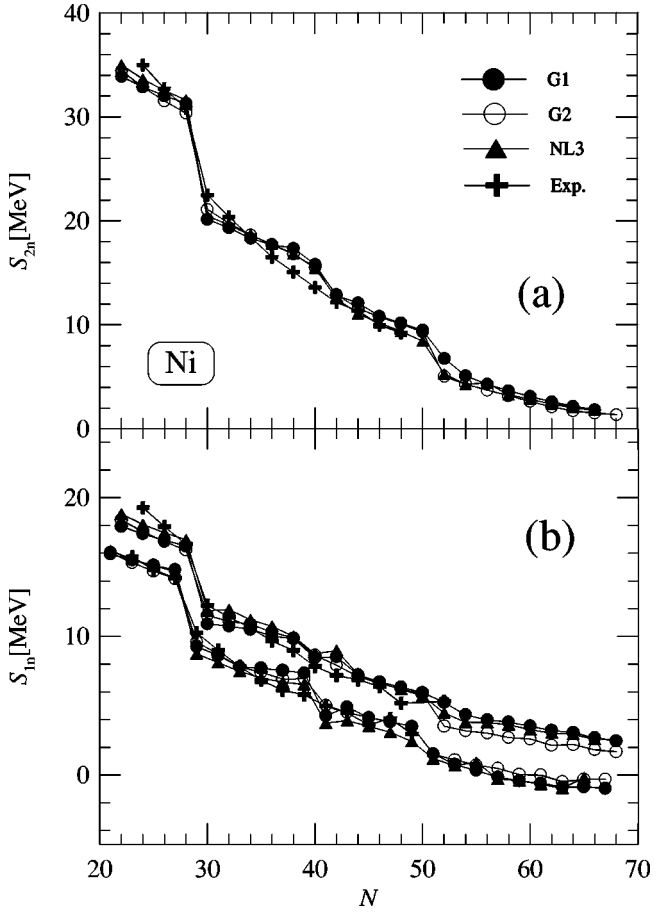

FIG. 6. Two-neutron (a) and one-neutron (b) separation energies for Ni isotopes computed with the qb-BCS approach for the parametrizations G1, G2, and NL3, in comparison with the experimental data.

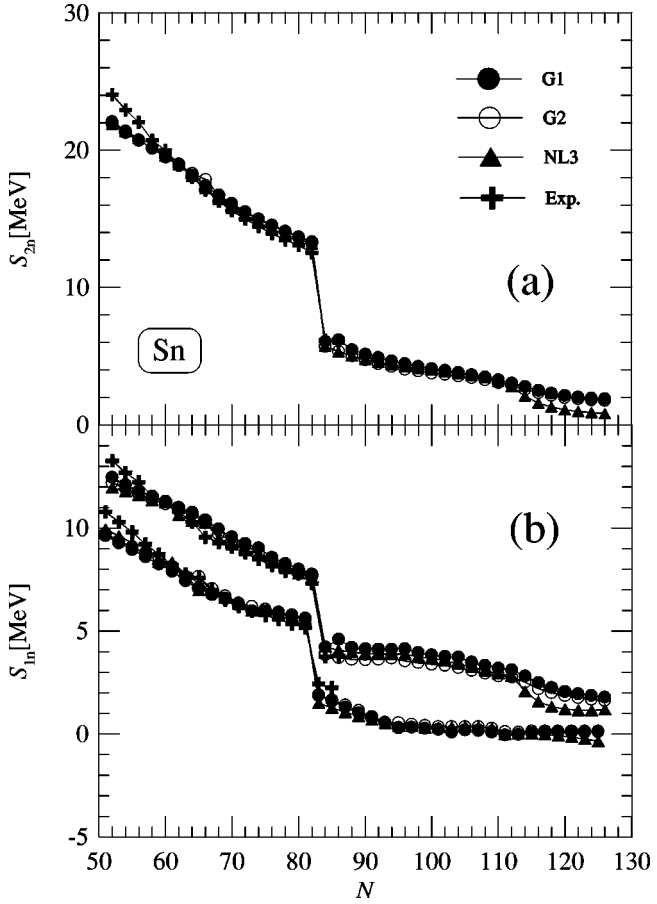

FIG. 7. Same as Fig. 6 for Sn isotopes.

ergies. In the case of the Ni isotopes we reach the drip line at $N=66$ with the G1 and NL3 sets and at $N=68$ with the G2 set. This agrees nicely with the value $N=66$ obtained in HFB calculations with the Skyrme forces SIII [34,45] and SkP [34]. For NL-SH our qb-BCS scheme predicts the drip line at $N=72$ [see Fig. 3(a)], the same value found in the RHB calculations of Ref. [35].

In Fig. 7(a) we display our qb-BCS results for the two-neutron separation energies of the Sn isotopic chain. In Ref. [32] it was claimed that pure BCS calculations in the constant gap approach (with NL3) are not suitable for the Sn isotopes. We observe in Fig. 7(a) that below $N=60$, as one moves towards $N=50$, some discrepancies with the experimental values appear, which also arise in the RHB calculations [32]. The three forces slightly overestimate the shell effect at $N=82$ (as the RHB results of Refs. [30,32] for NL3). We have computed Sn isotopes up to $A=176$, when S_{2n} vanishes for NL3 (in good agreement with RHB results for NL-SH [36] and HFB results for the Skyrme force SkP [23]). For G1 and G2 we find that S_{2n} does not yet vanish at $N=126$, and it is not possible to increase the neutron number due to the shell closure at $N=126$ (the neutron chemical potential becomes positive for the $N=128$ isotope). This means that the quenching of the shell effect at $N=126$ for NL3 (and NL-SH) is larger than for the G1 and G2 parameter sets.

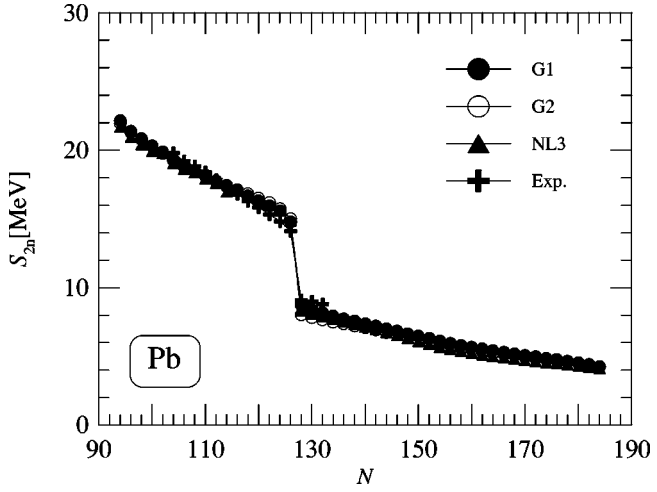

FIG. 8. Two-neutron separation energies for Pb isotopes computed with the qb-BCS approach, in comparison with experiment.

Our calculated S_{2n} energies for Pb isotopes are shown in Fig. 8. The experimental shell effect at $N=126$ is reasonably well reproduced by G1, G2, and NL3. The drip line is found at $N=184$ with a nonvanishing two-neutron separation energy, as in the calculations performed with the extended Skyrme force SLy4 in Ref. [38], where a similar approach (quasibound states and a state-dependent gap) to ours was used. The relatively large shell effect found at $N=184$ means that there is no quenching for this magic number in our qb-BCS approximation for the studied parameter sets. Indeed, to verify this point a full RHB calculation should be performed.

To analyze the proton pairing we have studied the two-proton separation energies in chains of isotones of $N=28$ [Fig. 9(a)] and $N=82$ [Fig. 10(a)]. In the case of $N=28$, shell gaps appear at $Z=20$ and $Z=28$. For $Z=20$ the predicted gap is larger than in experiment. For $Z=28$, G1 and G2 agree better than NL3 with experiment. S_{2p} vanishes at $Z=30$ for NL3, whereas it vanishes at $Z=32$ for G1 and G2. The isotones of $N=82$ display a clear shell effect at $Z=50$, in agreement with the nonrelativistic calculation of Ref. [38]. It is slightly larger for G2 than for G1 and NL3. Experimental information for this shell effect is not available. NL3 would predict another shell effect at $Z=58$, which does not appear experimentally. The effect is less pronounced in G1 and it does not show up in G2. The three forces indicate that the proton drip line is reached after the ^{156}W isotope, in agreement with experimental information [46].

Figures 11(a) and 11(b) show, respectively, the calculated S_{2p} separation energies for the $N=50$ and $N=126$ isotone chains. Note that we did not use any information about these nuclei in our fit of the G_p pairing strength. For $N=50$ the set G2 follows the experimental data very well, specially for the larger Z. The trend of G1 and NL3 is only a little worse. The proton drip line is located at ^{100}Sn in the three parametrizations, in good accordance with experiment. The quenching of the shell effect at $Z=50$ is larger for G2 than for G1 and NL3. The available data for two-proton separation energies of $N=126$ isotones are reasonably well estimated by the relativistic sets. However, the trend of NL3 is worse than that

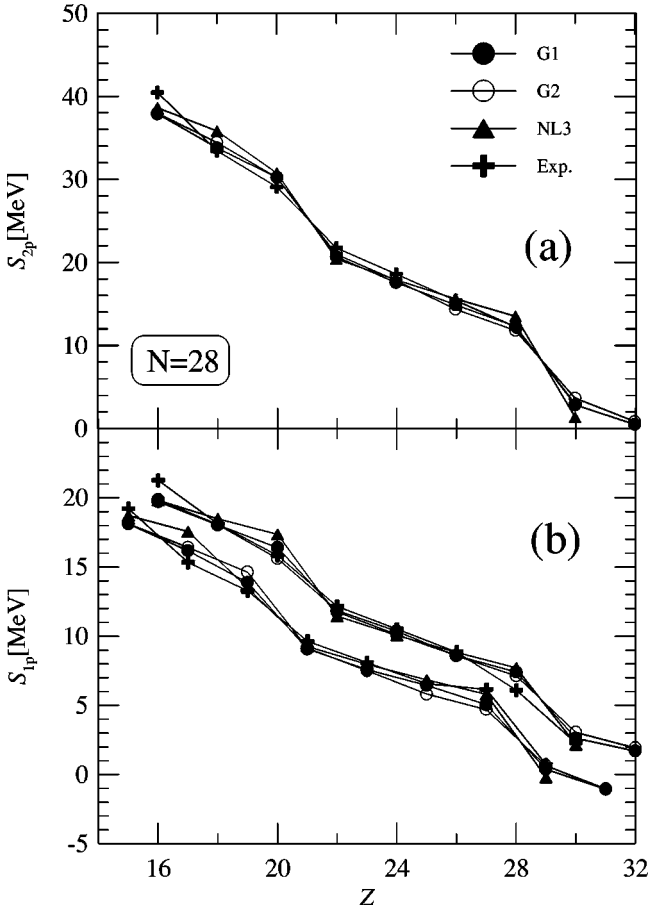

FIG. 9. Two-proton (a) and one-proton (b) separation energies for $N=28$ isotones computed with the qb-BCS approach, in comparison with experiment.

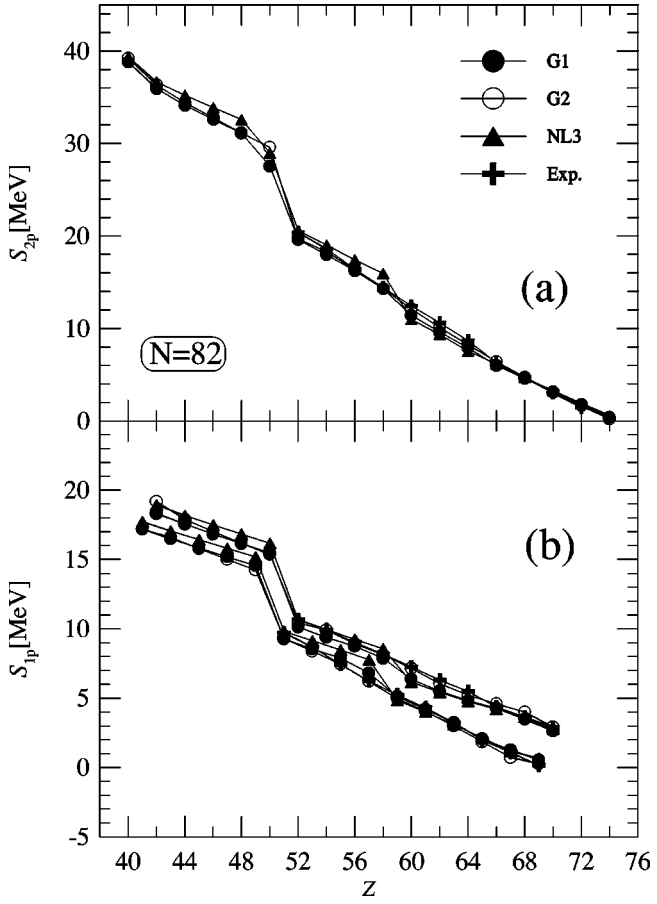

FIG. 10. Same as Fig. 9 for $N=82$ isotones.

of G1 and G2. It would then be very interesting to perform RHB calculations of this chain to confirm the behavior of NL3. The last nucleus of the chain stable against two-proton emission is ^{218}U according to G1 and NL3, and ^{220}Pu according to G2. The three sets predict a shell effect at $Z=92$, though it is relatively quenched for G2.

B. One-particle separation energies

We have computed one-neutron (one-proton) separation energies for Ni and Sn isotopes (for $N=28$ and $N=82$ isotones). The results are displayed in Figs. 6(b) and 7(b) [9(b) and 10(b)], respectively. To deal with odd mass number nuclei we have used a spherical blocking approximation. One pair of conjugate states $|\alpha\rangle$ and $|\tilde{\alpha}\rangle$ is blocked, i.e., taken out of the pairing scheme [25,26]. In the spherical approximation one replaces the blocked single-particle state by an average over the degenerate states in its j shell. This way the rotational and time-reversal invariance of the many-body system is restored in the intrinsic frame [47]. In this approach the contribution of the j shell that contains the blocked state to the number of active particles and the pairing energy is

$$A_j=(2j-1)n_j+1, \tag{12}$$

$$E_{\mathrm{pair},j}=-G\,(2j-1)[n_j(1-n_j)]^{1/2}, \tag{13}$$

respectively. The remaining active shells contribute in the usual manner [Eqs. (6) and (10)]. Due to rearrangement effects, blocking the single-particle state with smallest quasiparticle energy $E_\alpha=\sqrt{(\varepsilon_\alpha-\mu)^2+\Delta^2}$ in the even $A-1$ nucleus, does not necessarily lead to the largest binding energy of the odd A nucleus. Therefore in some cases one has to repeat the calculation blocking in turn the different single-particle states that lie around the Fermi level to find the configuration of largest binding energy [23,27,47].

The one-neutron (one-proton) separation energies lie over two different curves for even and odd neutron (proton) number. For Ni isotopes [Fig. 6(b)] the three parameter sets G1, G2, and NL3 reproduce reasonably the experimental values. The shell effect at $N=28$ is, again, overestimated by the three forces. The heaviest Ni isotope stable against one-neutron emission is found at $N=55$ with NL3 and G1 and at $N=57$ with G2. For Sn isotopes [Fig. 7(b)] the shell effect at $N=82$ is slightly overestimated by the studied forces. The predictions of the three parametrizations are roughly similar up to $N=110$, where the behavior of NL3 starts to depart from G1 and G2 due to the large quenching of the $N=126$ shell effect shown by NL3 as compared with G1 and G2. In our calculations, the odd Sn isotopes become unstable against the emission of one neutron around $N=110$. This value is larger than the values found with the nonrelativistic SkP interaction in HFB ($N=103$) or HF+BCS ($N=101$) calculations [23]. The origin of this discrepancy lies in the

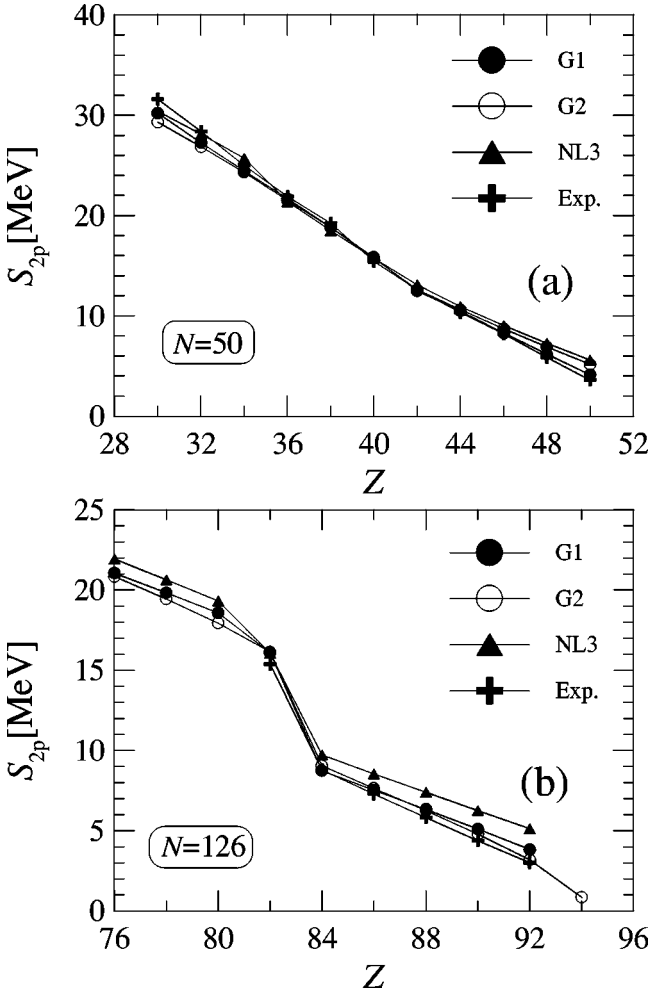

FIG. 11. Two-proton separation energies for $N=50$ (a) and $N=126$ (b) isotones computed with the qb-BCS approach, in comparison with experiment.

fact that the shell distribution in tin isotopes around $N=126$ for SkP is rather different from that of the relativistic sets [32].

The one-proton separation energies for the isotones of $N=28$ [Fig. 9(b)] show an overall good agreement with the experimental data. The shell effects at $Z=20$ and $Z=28$ are rather well reproduced by the forces analyzed here. G1 and G2 predict the heaviest nucleus stable against one-proton emission to be ^{57}Cu, as in experiment, while it is unstable in the NL3 calculation. For the isotones of $N=82$ [Fig. 10(b)] the shell effect predicted by NL3 and G1 at $Z=50$ is similar. Again, as for S_{2p} [Fig. 10(a)], NL3 predicts a shell effect at $Z=58$ which is not found experimentally, whereas for G1 this effect is clearly smaller and it does not appear for G2. The last stable nucleus against one-proton emission is ^{151}Tm according to the three parameter sets.

C. One-body densities and potentials

The nuclear densities for chains of isotopes of light and medium size nuclei have recently been studied in the RHB approximation [30,31,35,36]. As N grows the neutron and mass densities extend outwards and the rms radii and the surface thickness increase. Special attention has been paid to the isospin dependence of the spin-orbit interaction. The magnitude of the spin-orbit potential is reduced when one approaches the neutron drip line and, as a consequence, there is a reduction of the energy splittings between spin-orbit partner levels [30,31,36]. To our knowledge, for isotones such an study has only been carried out in the $N=20$ chain [31]. It is to be remarked that the EFT parametrizations G1 and G2 contain a tensor coupling of the ω meson to the nucleon which plays a very important role in the spin-orbit force because there exists a trade off between the size of this coupling and the size of the scalar field [15,17].

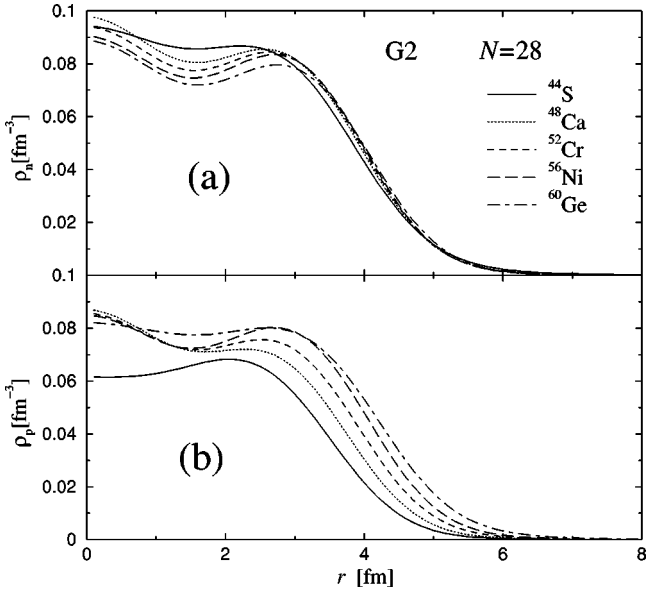

FIG. 12. Radial dependence of the neutron (a) and proton (b) densities of some $N=28$ isotones obtained with the G2 set.

In Figs. 12(a) and (b) we display, respectively, the neutron and proton densities of some $N=28$ isotones from $Z=16$ to $Z=32$ as predicted by the G2 set in our qb-BCS approach. Figures 13(a) and (b) show the results for some $N=82$ isotones from $Z=40$ to $Z=70$. Since N is fixed in each isotonic chain, the spatial extension of the neutron densities is very similar for the different nuclei of the chain. In any case, as one goes from the lightest to the heaviest isotone of the chain, the neutron densities tend to be depressed in the interior region and their surface thickness (90–10 % falloff distance) shows a decreasing tendency. The proton densities of the isotones exhibit a strong dependence on Z: by adding more protons they are raised at the interior and their surface is pushed outwards. For $N=28$ the surface thickness of ρ_p remains roughly constant up to $Z=28$ and increases for heavier isotones as a consequence of the growing occupation of the $1f_{7/2}$ shell. At the origin the proton densities show a bump when $Z\geqslant 20$ because the $2s_{1/2}$ level is occupied. The $Z=16$ isotone shows a dip at the center due to, precisely, the emptiness of this $2s_{1/2}$ level. For the considered nuclei of $N=82$, the proton densities have an approximately constant surface thickness and present a hole at the center owing to the Coulomb repulsion. In Fig. 14 we display the neutron

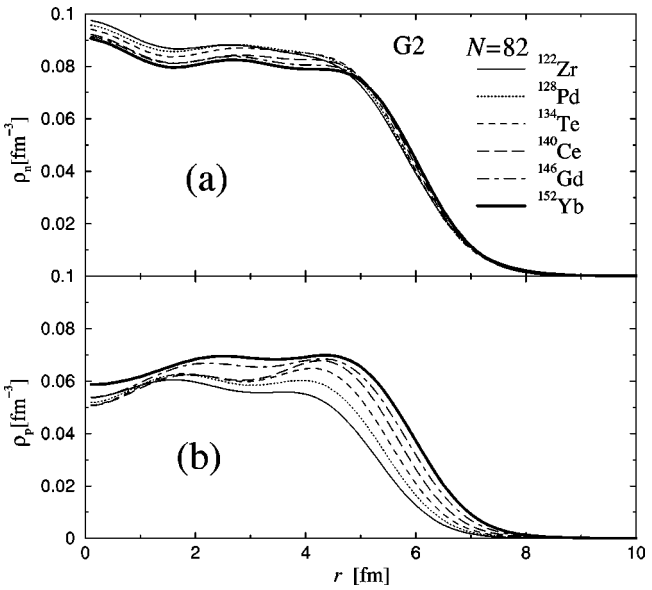

FIG. 13. Same as Fig. 12 for some $N=82$ isotones.

and proton rms radii of the $N=82$ isotonic chain obtained with G2 and NL3. It turns out that the predictions of both sets are very similar. The proton radii increase uniformly with Z, similarly to the behavior found for $N=20$ isotones with NL3 and the RHB scheme in Ref. [31]. The neutron radii remain roughly constant with Z. They just show a slight decrease with increasing Z till $Z\sim 50$ and slightly increase afterwards. This behavior may be related with the shell effect for protons at $Z=50$.

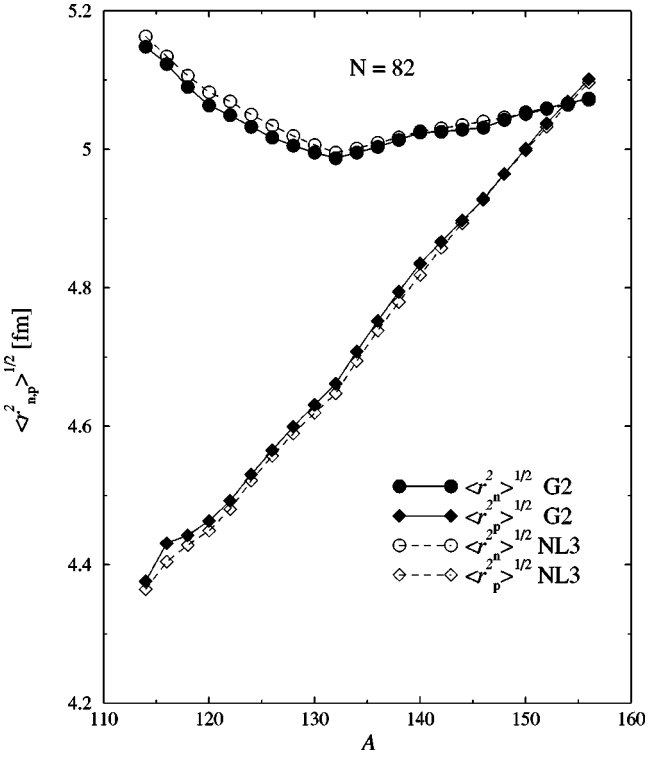

FIG. 14. Neutron and proton rms radii of $N=82$ isotones obtained with the G2 and NL3 sets.

The spin-orbit interaction is automatically included in the RMF approximation. It appears explicitly when the lower spinor of the relativistic wave function is eliminated in favor of the upper spinor. This way one obtains a Schrödinger-like equation with a term $V_{SO}(r)$ that has the structure of the single-particle spin-orbit potential. Including the contribution of the tensor coupling of the ω meson, the spin-orbit term reads [15,30]

$$H_{SO}=\frac{1}{2M^2}V_{SO}(r)\,\mathbf{L}\cdot\mathbf{S}, \tag{14}$$

$$V_{SO}(r)=\frac{M^2}{\bar{M}^2}\frac{1}{r}\left(\frac{d\Phi}{dr}+\frac{dW}{dr}\right)+2f_v\frac{M}{\bar{M}}\frac{1}{r}\frac{dW}{dr}, \tag{15}$$

where $\bar{M}=M-\frac{1}{2}(\Phi+W)$. We have checked numerically that the contribution to the spin-orbit potential of the f_ρ tensor coupling of the ρ meson is very small, even when one approaches the drip lines. Hence we have not written this contribution in Eq. (15).

The spin-orbit potential (15) for some lead isotopes computed with G2 and NL3 is displayed in Figs. 15(a) and (b), respectively. As a general trend, for both G2 and NL3, when the number of neutrons is increased the depth of the spin-orbit potential decreases gradually and the position of the bottom of the well is shifted outwards, which implies a significant weakening of the spin-orbit interaction. The same effect arises in other isotopic chains in RHB calculations [30,35,36]. Comparing the spin-orbit potentials obtained with the G2 and NL3 sets, one sees that they have a similar strength for all the isotopes analyzed and that the minima of the wells are located at similar positions (slightly shifted to larger values of r in G2). The higher effective mass of G2 at saturation ($M^*_\infty/M=0.664$) with respect to NL3 ($M^*_\infty/M=0.595$) is compensated by the tensor coupling included in G2 ($f_v=0.692$). To ascertain the relative importance of the tensor coupling we have drawn in the insert of Fig. 15(a), for ^{228}Pb, the full potential (15) and the contribution resulting from setting $f_v=0$ in Eq. (15). We see that the full $V_{SO}(r)$ is much deeper and wider. The maximum depth of $V_{SO}(r)$ changes from -68 MeV fm^{-2} (right scale of the insert) to -44 MeV fm^{-2} when $f_v=0$. That is, the tensor coupling accounts for roughly one-third of the total spin-orbit strength in the G2 parameter set.

One expects that the weakening of the spin-orbit potential in going to the neutron drip line will bring about a reduction of the spin-orbit splittings

$$\Delta\varepsilon=\varepsilon_{nl,j=l-1/2}-\varepsilon_{nl,j=l+1/2} \tag{16}$$

of the neutron levels [30]. Figure 16 displays the energy splittings of some spin-orbit partner levels of neutrons for lead isotopes, obtained with the G2 and NL3 parameter sets. The splittings predicted by G2 and NL3 are very close as a consequence of the similarity of the corresponding spin-orbit potentials. Partner levels with high angular momentum undergo some reduction in the splitting along the Pb isotopic chain, but partners with small angular momentum show an

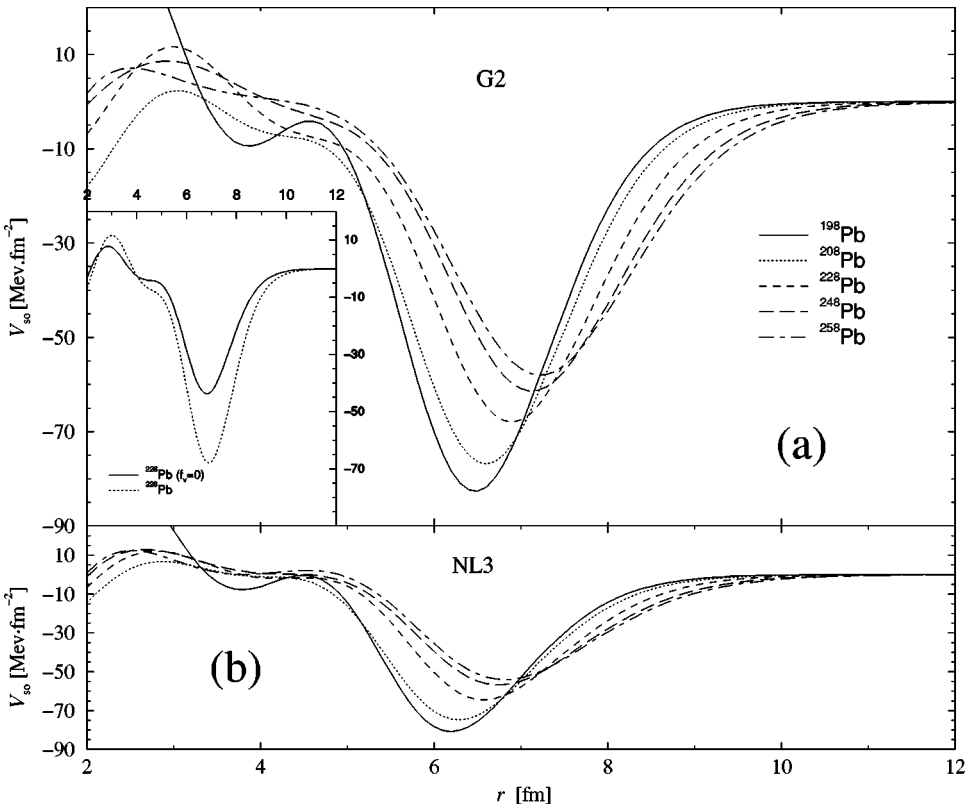

FIG. 15. Spin-orbit potential for some Pb isotopes obtained with the G2 set (a) and with the NL3 set (b).

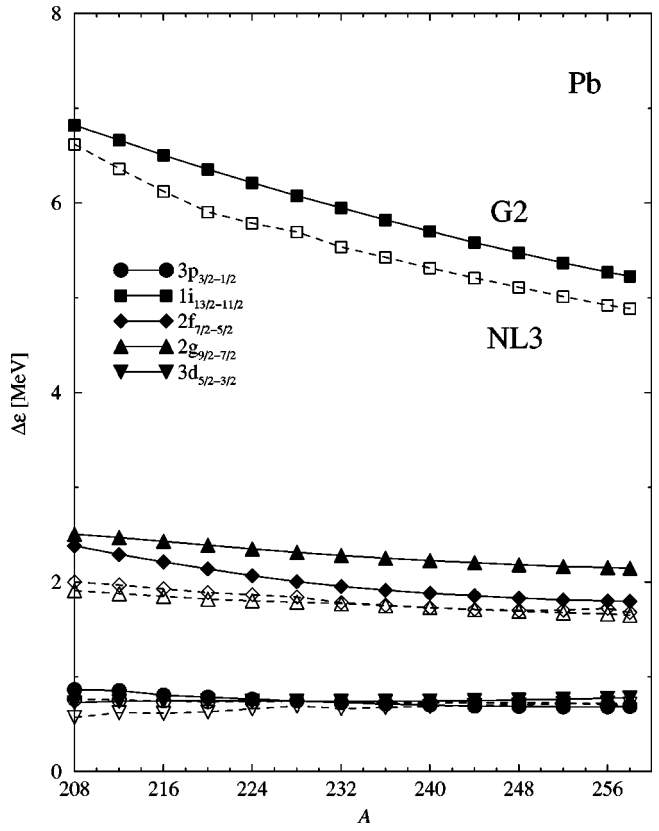

FIG. 16. Energy splitting of some spin-orbit partner levels of neutrons in Pb isotopes, calculated in the qb-BCS approach for the G2 and NL3 sets.

almost constant splitting. By comparison of their RHB results for Ni and Sn, the authors of Ref. [30] pointed out that the weakening of the spin-orbit interaction should be less important for heavier isotopic chains. Our calculations for Pb would confirm this statement. All the single-particle levels involved in Fig. 16 are bound. Of course, one should not expect the results for $\Delta\varepsilon$ to be so reliable in our qb-BCS approach if one, or both, of the partner levels lies at positive energy. The reason is that the single-particle energies of the quasibound levels do not exactly reproduce the energies of the corresponding canonical states of a RHB calculation.

In Figs. 17(a) and (b) we show the spin-orbit potential for isotones of $N=82$ from $Z=40$ to $Z=70$, for the G2 and NL3 parametrizations. Similarly to what is found for isotopes, the results obtained from G2 and from NL3 are comparable and the spin-orbit potential well $V_{SO}(r)$ moves outwards with the addition of protons, following the tendency of the proton density. However, for isotones we find that the behavior of the depth of the spin-orbit potential well is not so monotonous: it increases when one goes from the neutron drip line up to the β-stable region, while it decreases afterwards as more protons are added.

V. SUMMARY AND CONCLUSION

We have analyzed the pairing properties of some chains of isotopes and isotones with magic Z and N numbers in the relativistic mean field approach. The study has been performed for the G1 and G2 parametrizations that were obtained in Ref. [10] from the modern effective field theory approach to relativistic nuclear phenomenology. We have compared the results with those obtained with the NL3 pa-

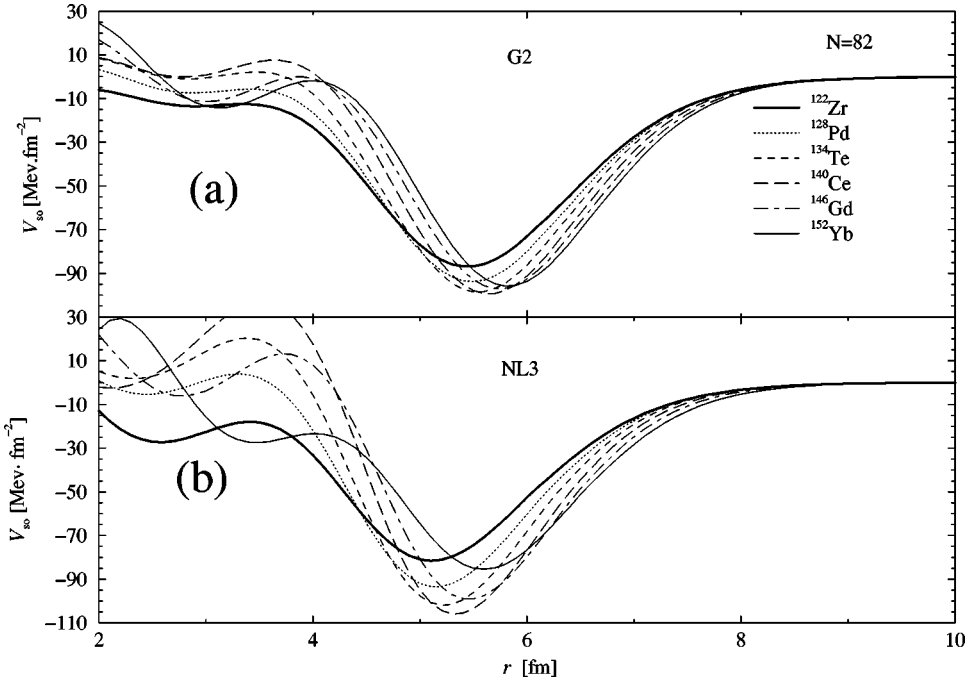

FIG. 17. Spin-orbit potential for some $N=82$ isotones obtained with the G2 set (a) and with the NL3 set (b).

rameter set which is considered to be very successful for dealing with nuclei beyond the stability line.

For accurate calculations of pairing far from the valley of β stability in the relativistic models, the relativistic Hartree-Bogoliubov approach should be applied. However, we have presented a simpler modified BCS approach which allows one to obtain pairing properties near the drip lines fast and confidently. The method has been used previously in nonrelativistic calculations with Skyrme forces [38,39]. The key ingredient is to take into account the continuum contributions through quasibound levels due to their centrifugal barrier. To further simplify the calculations we have assumed pairing matrix elements of the type $G=C/A$ instead of, e.g., a state-dependent pairing with a zero-range force.

The considered quasibound levels are mainly localized in the classically allowed region and decrease exponentially outside it. This eliminates the unphysical nucleon gas which, near the drip lines, surrounds the nucleus when all available positive energy levels are included in the usual BCS approach. Normally, the quasibound levels have high angular momentum and lie close in energy to the corresponding RHB canonical levels. One of the limitations of the qb-BCS approach employed here is the fact that the nuclear density does not follow the asymptotic falloff of the densities computed with the relativistic Hartree-plus-Bogoliubov theory. In spite of this shortcoming, we have shown by comparison with available RHB results that the qb-BCS approach is able to predict the position of the drip lines, or the behavior of the neutron and charge radii for nuclei far from the stability line, in a reasonable way. Also, the obtained pairing gaps are nicely scattered around the empirical average $12/\sqrt{A}$.

We have applied the qb-BCS approach to the Ni, Sn, and Pb isotopic chains, and to the $N=28$, 50, 82, and 126 isotonic chains. The two-neutron (two-proton) and one-neutron (one-proton) separation energies, as well as the resulting shell gaps, are similar for the three studied relativistic parametrizations (G1, G2, and NL3) and in general they reproduce the available experimental data, at least qualitatively. The neutron and proton drip lines are usually reached at the same place with the three forces, though one may find a shift of one or two units of A among them. We have paid some attention to the quenching of the shell structure near the drip lines. For example, the quenching of the shell effect at $N=126$ for Sn isotopes is larger in NL3 than in G1 and G2, while for Pb isotopes none of the three sets exhibits a quenching of the shell effect at $N=184$ in our qb-BCS calculation. The EFT parametrizations G1 and G2 contain tensor couplings that are not present in the RMF parametrizations like NL3 and have a larger effective mass at saturation. However, the predicted spin-orbit potentials along the isotopic and isotonic chains do not differ much from those obtained with NL3.

Our analysis shows that the parameter sets based on EFT are able to describe nuclei far from the β-stability line, after adding a phenomenological pairing residual interaction. Only experimental information about some magic nuclei was utilized in the fit of the constants of the G1 and G2 sets and thus the results for nuclei near the drip lines are veritable predictions of the model. In spite of the fact that the EFT sets include more couplings and parameters than the conventional RMF sets like NL3, both models reproduce the experimental systematics with a similar quality. In fact, the studied properties away from the valley of β stability do not seem to provide further constraints on the EFT parameters, not even in the isovector sector. In conclusion, extended sets like G1 and G2 will serve almost the same purposes for normal systems as the conventional parameter sets. However, some of the extra parameters of the general EFT functional may be used to better describe regions of the equation of state at higher density or temperature [16,18] without spoiling the systematics for finite nuclei.

ACKNOWLEDGMENTS

The authors would like to acknowledge support from the DGICYT (Spain) under Grant No. PB98-1247 and from DGR (Catalonia) under Grant No. 1998SGR-00011. S.K.P. thanks the Spanish Education Ministry, Grant No. SB97-OL174874, for financial support and the Departament d'Estructura i Constituents de la Matèria of the University of Barcelona for kind hospitality.

[1] B. D. Serot and J. D. Walecka, Adv. Nucl. Phys. **16**, 1 (1986).
[2] P.-G. Reinhard, Rep. Prog. Phys. **52**, 439 (1989).
[3] B. D. Serot, Rep. Prog. Phys. **55**, 1855 (1992).
[4] B. D. Serot and J. D. Walecka, Int. J. Mod. Phys. E **6**, 515 (1997).
[5] Y. K. Gambhir, P. Ring, and A. Thimet, Ann. Phys. (N.Y.) **198**, 132 (1990).
[6] P. Ring, Prog. Part. Nucl. Phys. **37**, 193 (1996).
[7] J. D. Walecka, Ann. Phys. (N.Y.) **83**, 491 (1974).
[8] J. Boguta and A. R. Bodmer, Nucl. Phys. **A292**, 413 (1977).
[9] R. J. Furnstahl, B. D. Serot, and H. B. Tang, Nucl. Phys. **A598**, 539 (1996).
[10] R. J. Furnstahl, B. D. Serot, and H. B. Tang, Nucl. Phys. **A615**, 441 (1997).
[11] H. Müller and B. D. Serot, Nucl. Phys. **A606**, 508 (1996).
[12] J. J. Rusnak and R. J. Furnstahl, Nucl. Phys. **A627**, 495 (1997).
[13] R. J. Furnstahl and B. D. Serot, Nucl. Phys. **A671**, 447 (2000).
[14] B. C. Clark, R. J. Furnstahl, L. K. Kerr, J. Rusnak, and S. Hama, Phys. Lett. B **427**, 231 (1998).
[15] R. J. Furnstahl, J. J. Rusnak, and B. D. Serot, Nucl. Phys. **A632**, 607 (1998).
[16] P. Wang, Phys. Rev. C **61**, 054904 (2000).
[17] M. Del Estal, M. Centelles, and X. Viñas, Nucl. Phys. **A650**, 443 (1999).
[18] M. Del Estal, M. Centelles, X. Viñas, and S. K. Patra, Phys. Rev. C **63**, 024314 (2001).
[19] *Proceedings of the International Conference on Exotic Nuclei and Atomic Masses: ENAM 95*, Arles, France, 1995, edited by M. de Saint-Simon and O. Salen (Editions Frontières, Gif-sur-Yvette, 1995).
[20] Z. Patyk, A. Baran, J. F. Berger, J. Dechargé, J. Dobaczewski, P. Ring, and A. Sobiczewski, Phys. Rev. C **59**, 704 (1999).
[21] P.-G. Reinhard, M. Rufa, J. Maruhn, W. Greiner, and J. Friedrich, Z. Phys. A **323**, 13 (1986).
[22] Y. Sugahara and H. Toki, Nucl. Phys. **A579**, 557 (1994).
[23] J. Dobaczewski, H. Flocard, and J. Treiner, Nucl. Phys. **A422**, 103 (1984).
[24] J. Dobaczewski, W. Nazarewicz, T. R. Werner, J. F. Berger, R. C. Chin, and J. Dechargé, Phys. Rev. C **53**, 2809 (1996).
[25] J. M. Eisenberg and W. Greiner, *Microscopic Theory of the Nucleus* (North-Holland, Amsterdam, 1972).
[26] P. Ring and P. Schuck, *The Nuclear Many-Body Problem* (Springer-Verlag, Berlin, 1980).
[27] J. Dechargé and D. Gogny, Phys. Rev. C **21**, 1568 (1980).
[28] H. Kucharek and P. Ring, Z. Phys. A **339**, 23 (1991).
[29] T. Gonzalez-Llarena, J. L. Egido, G. A. Lalazissis, and P. Ring, Phys. Lett. B **379**, 13 (1996).
[30] G. A. Lalazissis, D. Vretenar, and P. Ring, Phys. Rev. C **57**, 2294 (1998).
[31] D. Vretenar, G. A. Lalazissis, and P. Ring, Phys. Rev. C **57**, 3071 (1998).
[32] M. M. Sharma, A. R. Farhan, and S. Mythili, Phys. Rev. C **61**, 054306 (2000).
[33] J. F. Berger, M. Girod, and D. Gogny, Nucl. Phys. **A428**, 32 (1984).
[34] J. Terasaki, P.-H. Heenen, P. Bonche, J. Dobaczewski, and H. Flocard, Nucl. Phys. **A593**, 1 (1995).
[35] J. Meng, Phys. Rev. C **57**, 1229 (1998); Nucl. Phys. **A635**, 3 (1998).
[36] J. Meng and I. Tanihata, Nucl. Phys. **A650**, 176 (1999).
[37] F. Tondeur, Nucl. Phys. **A315**, 353 (1979).
[38] E. Chabanat, P. Bonche, P. Haensel, J. Meyer, and R. Schaeffer, Nucl. Phys. **A635**, 231 (1998).
[39] N. Sandulescu, Nguyen Van Giai, and R. J. Liotta, Phys. Rev. C **61**, 061301(R) (2000).
[40] S. J. Krieger, P. Bonche, H. Flocard, P. Quentin, and M. S. Weiss, Nucl. Phys. **A517**, 275 (1990).
[41] G. A. Lalazissis, J. König, and P. Ring, Phys. Rev. C **55**, 540 (1997).
[42] G. Baym, Phys. Rev. **117**, 886 (1960).
[43] M. M. Sharma, M. A. Nagarajan, and P. Ring, Phys. Lett. B **312**, 377 (1993).
[44] A. Bohr and B. R. Mottelson, *Nuclear Structure* (Benjamin, New York, 1969), Vol. I.
[45] J. Terasaki, P.-H. Heenen, H. Flocard, and P. Bonche, Nucl. Phys. **A600**, 371 (1996).
[46] R. D. Page, P. J. Woods, R. A. Cunningham, T. Davinson, N. J. Davis, S. Hofmann, A. N. James, K. Livingston, P. J. Sellin, and A. C. Shotter, Phys. Rev. Lett. **68**, 1287 (1992).
[47] B. Bender, K. Rutz, P.-G. Reinhard, and J. A. Maruhn, Eur. Phys. J. A **8**, 59 (2000).